Time-lapse analysis of ambient surface wave anisotropy:
A three-component array study above
an underground gas storage

Nima Riahi,[1] Götz Bokelmann,[2] Paola Sala,[3] and Erik H. Saenger[1]

[1] We perform a time-lapse analysis of Rayleigh and Love wave anisotropy above an underground gas storage facility in the Paris Basin. The data were acquired with a three-component seismic array deployed during several days in April and November 2010. Phase velocity and back azimuth of Rayleigh and Love waves are measured in the frequency range 0.2–1.1 Hz using a three-component beamforming algorithm. In both snapshots, higher-surface wave modes start dominating the signal above 0.4 Hz with a concurrent increase in back azimuth ranges. We fit anisotropy parameters to the array detections above 0.4 Hz using a bootstrap approach which also provides estimation uncertainty and enables significance testing. The isotropic phase velocity dispersion for Love and Rayleigh waves match for both snapshots. We also observe a stable fast direction of NNW-SSE for Love and Rayleigh waves which is aligned with the preferred orientation of known shallow (<300 m) and deeper (~1000 m) fault systems in the area, as well as the maximum horizontal stress orientation. At lower frequencies corresponding to deeper parts of the basin, the anisotropic parameters exhibit higher magnitude in the November data. This may perhaps be caused by the higher pore pressure changes in the gas reservoir in that depth range.

1. Introduction

[2] Sensing seismic anisotropy in the crust and upper mantle provides important constraints on deformation and forces acting within the solid Earth [*Maupin and Park*, 2007]. Both body waves and surface waves have been frequently used for measuring such anisotropy over the last decades [*Wüstefeld et al.*, 2009]. A still novel field in this respect is the application of array techniques for that purpose. This has been introduced for *P* waves by *Bokelmann* [1995] who had used array analysis together with polarization of *P* waves to constrain seismic anisotropy in the crust. *Bear et al.* [1999] had embedded such an approach in a three-component array-processing procedure. Since surface waves provide good depth resolution, it is highly desirable to establish such an approach for surface waves, which is also natural considering the rich polarization properties of surface waves.

[3] Numerous studies have addressed seismic anisotropy using surface waves [*Maupin and Park*, 2007], and more recently using ambient noise as a new data source to probe such anisotropy. The ambient seismic wave field is attractive because it carries significant seismic surface wave energy and is usually also available where natural seismicity is low. Many noise studies analyze seismic cross correlations, often in combination with tomographic inversion, to produce maps of seismic anisotropy in the subsurface [*Shapiro et al.*, 2004; *Moschetti et al.*, 2010; *Fry et al.*, 2010; *Schaefer et al.*, 2011; *Gallego et al.*, 2011; *Pawlak et al.*, 2012; *Adam and Lebedev*, 2012]. Such techniques were also applied to study anisotropy changes after large earthquakes [*Durand et al.*, 2011; *Nakata and Snieder*, 2012; *Takagi and Okada*, 2012; *Tonegawa et al.*, 2013]. *Alvizuri and Tanimoto* [2011] used array analysis on teleseismic Rayleigh waves in Southern California to compute azimuthal anisotropy, but noise analyses with arrays are generally focused more on isotropic velocity structure inversion [*Scherbaum et al.*, 2003; *Kind et al.*, 2005; *Parolai et al.*, 2005; *Wathelet et al.*, 2005] and the study of oceanic microseism source mechanisms [*Bromirski and Duennebier*, 2002; *Gerstoft et al.*, 2006, 2008; *Koper and de Foy*, 2008; *Koper et al.*, 2009; *Zhang et al.*, 2009, 2010; *Landes et al.*, 2010]. However, such studies generally do not make full use of the polarization properties, and we will show in this paper that including that information can be rather useful.

[1]Earth Science Department, ETH Zurich, Zurich, Switzerland.
[2]Department of Meteorology and Geophysics, University of Vienna, Vienna, Austria.
[3]Institute of Geological Sciences, University of Berne, Berne, Switzerland.

Corresponding author: N. Riahi, Earth Science Department, ETH Zurich, Sonneggstrasse 5, 8092 Zurich, Switzerland. (nima.riahi@erdw.ethz.ch)

[4] We analyze ambient seismic data acquired above an underground gas storage (UGS) facility about 170 km southwest of Paris during a few days in April and November 2010. This represents two wave field snapshots of not only Spring and Autumn but also of a low-pressure and high-pressure state of the UGS reservoir. The data were acquired in the frequency range 0.1–1.1 Hz where substantial energy from microseisms dominate the wave field and where nonnegligible sensitivity to the storage reservoir can be expected. Our objective is to use frequency domain beamforming to test if the two snapshots differ in surface wave anisotropy at the surface, a phenomenon that might be linked to changes in the storage reservoir. The statistical variability in the beamformer estimates due to uncontrolled factors are taken into account by considering bootstrap-based uncertainty assessments on the anisotropy parameters.

[5] Our results show that ambient surface wave anisotropy generally exhibits a fast axis roughly parallel to the preferred orientation of local fault systems. However, we observe that the anisotropy magnitude increases at lower frequencies in November. Pore pressure variations in the reservoir could plausibly be responsible for the observed change, although other causes cannot be ruled out. This study shows how array processing of the higher-frequency flank of microseisms may open interesting possibilities for monitoring applications in the shallow crust and in sedimentary basins.

[6] In section 2 we describe the geological setting of the study area and the data acquisition. Three-component array beamforming is explained in section 3. An overview of the array detections is given in section 4. Section 5 describes how the anisotropy parameters were fitted and shows the results for both snapshots. Discussion and conclusions follow in sections 6 and 7.

2. Geology of Study Area and Data Acquisition

[7] The Paris Basin is a broad and circular intracratonic basin filled with sediments at low regional dips (on average less than 1°). The basin developed mostly during the Mesozoic and was affected by numerous deformation phases in the Tertiary. Deep fault systems are known to affect a large part of the stratigraphic column, from the deep Permo-Carboniferous levels up to Cenozoic levels [*Debeglia and Debrand Passard*, 1980; *Beccaletto et al.*, 2011]. Some of these faults were reactivated during later tectonic phases, and their orientation was inherited up to the shallow subsurface. Similar fault orientations can therefore be observed at different depths.

[8] Our study area is located 170 km southwest of Paris near Chémery and lies above an underground gas storage (UGS) facility that is operating since the 1970s. The Chémery area is situated in one of the deepest parts of the Paris Basin with a sedimentary thickness above the basement of up to 2.6 km [*Perrodon and Zabek*, 1990]. The sedimentary sequence mainly consists of limestone, dolomite, shale, and fluvial sandstones. The gas reservoir levels are located below 1085 m depth and may have a thickness of up to 100 m [*Hamon and Merzeraud*, 2005]. They are known to be affected by NNW-SSE and east-west fault systems, as seen on a map of the Triassic sandstone shown in *Fleury et al.* [1997]. Some of the faults propagate through the entire sedimentary sequence up to the surface as suggested by a west-east cross section in *Fleury et al.* [1997]. Therefore, the same fault system is also recognizable in shallow formations and was recently reconstructed in a three-dimensional geological model [*Sala et al.*, 2013]. Figure 1 shows a map of the study area with the shallow and deeper fault systems.

[9] We analyze data acquired with a temporary seismic three-component array with a rectangular aperture of 3×6 km and consisting of 80–85 seismometers. The array was deployed during four days in April (effective operation 65 h) and eight days in November 2010 (effective operation 55 h). The Chémery UGS is France's largest gas storage facility and although precise pore pressure information was not available to us, it is known that in April it was close to its lowest pore pressure due to Winter gas extraction while in November it was close to its maximum pore pressure after gas injection during the warmer months. The red triangles in Figure 1 show a typical array geometry from 22 April.

[10] The acquisition geometry changed three times during each of the acquisition periods. This led to eight-array geometries that shared the same aperture (3×6 km) and interstation spacing (about 500 m) but had slightly different internal configurations due to permitting constraints and sensor failure. The variations in the array beam patterns, however, were negligible and also afforded a spatial sampling with little aliasing issues below 1 Hz. The seismic wave field was sensed using broadband seismometers with a sensitivity of 1500 V/(m/s) and a relatively flat frequency response above 0.03 Hz. The cutoff frequency due to the sampling rate was 50 Hz. The sensors were placed in small holes of about 50 cm depth, oriented toward magnetic North using a hand compass, and covered with a wooden board to reduce wind noise and interactions with local fauna.

[11] For a small fraction of the receivers, one or more components deviated strongly from the rest of the array members. These stations were removed from the analysis. Using teleseismic earthquake arrivals, one recording was found to have a time shift of 2.6 sec and was corrected accordingly.

3. Three-Component Array Processing

[12] The frequency wave number technique has been successfully applied in many applications of seismic noise ranging from microseism studies [e.g., *Toksoz and Lacoss*, 1968; *Gerstoft et al.*, 2008] to subsurface velocity inversion [e.g., *Scherbaum et al.*, 2003; *Kind et al.*, 2005]. The technique extracts back azimuths and phase velocities of coherent wave trains as a function of frequency, thus providing a detailed characterization of the seismic wave field at the array location. We first give a brief formulation of this technique for single-component arrays and then show how it can be extended to additionally decompose polarization for seismic three-component arrays.

3.1. Single-Component Array

[13] For a single-component, say vertical, array the Fourier amplitudes of the signals on all M array sensors are summarized as a data vector $\mathbf{s} = [s_1, s_2, \ldots, s_M]^T$ (the frequency dependence will not be explicitly stated in
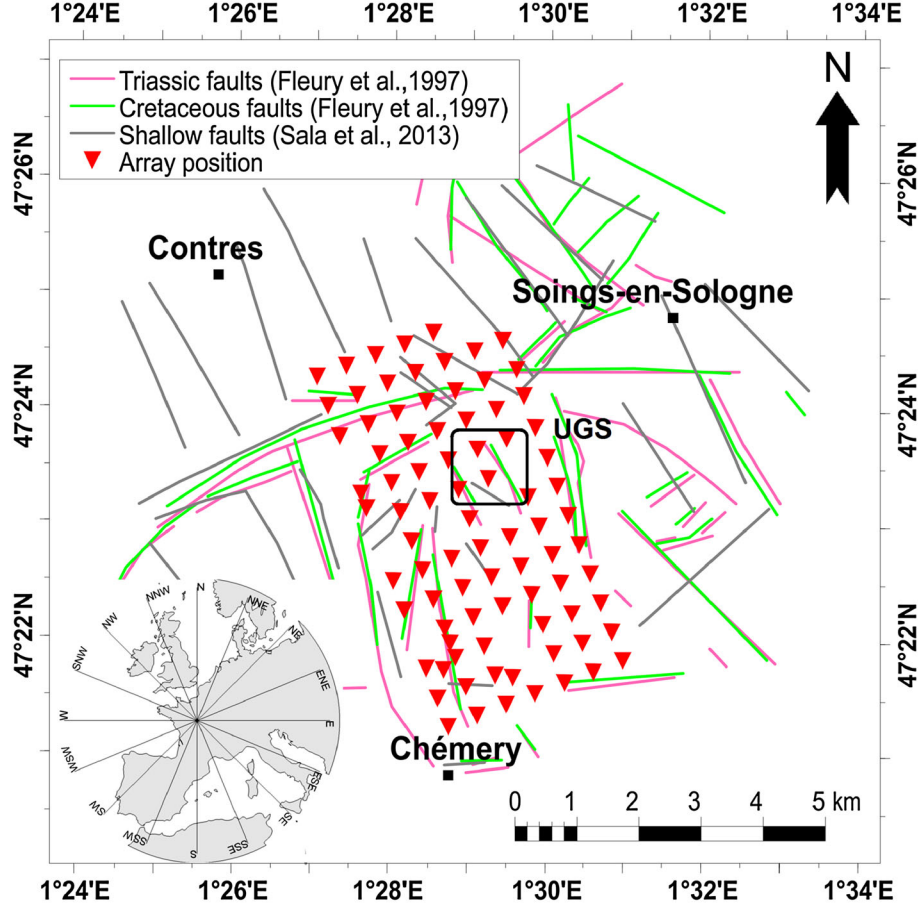
Figure 1. Map of the study area. The solid lines show fault systems characterized by *Sala et al.* [2013] (<300 m, gray) and *Fleury et al.* [1997] (1 km, red and green). The square shows the approximate location of the main UGS facilities and the triangles indicate the locations of the broadband seismometers on 22 April. The inlet shows an orthographic map of the region around the array.

the following equations). The relative phase shifts between these M signals are captured by the spectral density matrix $\mathbf{S} = \langle \mathbf{s} \cdot \mathbf{s}^{\dagger} \rangle$, where $\langle \; \rangle$ stands for the time ensemble operation. The diagonal elements s_{ii} are real and estimate the power spectral density of the signal on sensor i, while the off-diagonal elements s_{ij} are complex and estimate the cross-spectral power density between sensors i and j. The phase and amplitude of s_{ij} corresponds to the relative phase difference between the sensors and the product of the expected amplitudes on the sensors. Note that $\mathbf{S}$ is therefore hermitian.

[14] A typical model for a coherent signal across the array is the plane wave. The complex magnitude of the plane wave for a location $\mathbf{r}$ and time t is

$$x(\mathbf{r}, t) = A \cdot \exp[2\pi i (\mathbf{k} \cdot \mathbf{r} - ft)], \qquad (1)$$

where $\mathbf{k}$ is the wave vector of the plane wave with a magnitude $1/\lambda$ and pointing in the direction of propagation (km^{-1}), f is the frequency of the plane wave oscillation in time (Hz), and A is a complex scalar describing the amplitude and phase of the plane wave. The theoretical phases and amplitudes observed on the M signals of the array by such a passing plane wave are captured in the so-called mode vector or array response vector. This is a complex M-dimensional vector parameterized by the wave vector, $\mathbf{k}$:

$$\mathbf{a}(\mathbf{k}) = \frac{1}{\sqrt{(M)}} \begin{bmatrix} \exp(2\pi i \, \mathbf{k} \cdot \mathbf{r}_1) \\ \vdots \\ \exp(2\pi i \, \mathbf{k} \cdot \mathbf{r}_M) \end{bmatrix}, \qquad (2)$$

where $\mathbf{r}_n$ are the coordinates of sensor n in the array plane and the factor $1/\sqrt{(M)}$ normalizes $\mathbf{a}$ to unit length. For a single-component array the vector elements vary only in complex phase, not amplitude. In conventional beamforming, given the observed phase variations in $\mathbf{S}$, the response of the array signals as a function of $\mathbf{k}$ is computed as

$$R(\mathbf{k}) = \mathbf{a}(\mathbf{k})^{\dagger} \cdot \mathbf{S} \cdot \mathbf{a}(\mathbf{k}). \qquad (3)$$

[15] The response $R(\mathbf{k})$ is maximized when $\mathbf{k}$ matches with the wave vector of an actual plane wave impinging on the array [*Lacoss et al.*, 1969]. In an asymptotic sense (very large arrays), this result also applies when there are several sources, each having an arbitrary stochastic time signal and mixed with random noise. However, sufficient time must be recorded to reduce the variance of the estimations. The effect of array geometry on beamforming estimates is mainly controlled by the array response pattern which is the beam response to a signal that has the same phase on all receivers (i.e., infinite velocity). Figure 2 shows the response of the array operating on 22 April. The central
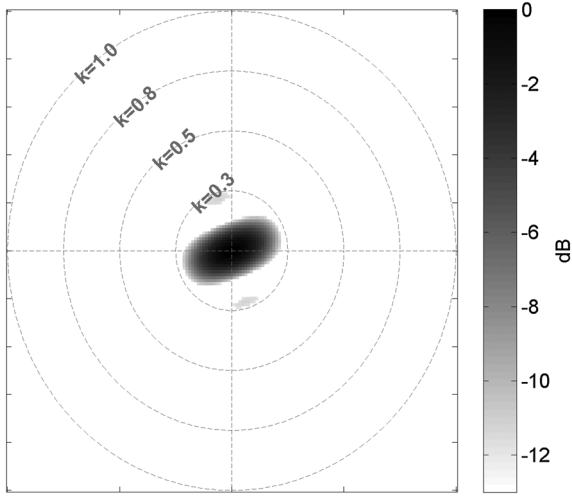
Figure 2. Array response for the array geometry shown in Figure 1 (units are in kilometers). Besides the main lobe in the center four weak (< –12 dB) sidelobes were present. Since the array geometry did not change substantially, this response remained essentially the same for all acquisition days.

peak controls the beamformer resolution in wave number space and side lobes indicate potential leakage to other wave vectors. These aspects are discussed further below. As mentioned in section 2, the variations in the array responses of the eight-array configurations present during the study were negligible.

3.2. Three-Component Array

[16] Our formulation of the three-component array is closely related to that of *Esmersoy et al.* [1985]. For the case of a three-component array, let the frequency domain data vector of the $M \cdot 3$ array signals be

$$\mathbf{s}_{3C} = [s_{E,1}, \ldots, s_{E,M}, s_{N,1}, \ldots, s_{N,M}, s_{V,1}, \ldots, s_{V,M}]^T, \quad (4)$$

where $s_{\{E,N,V\},n}$ is the Fourier amplitude of the signal on the east, north, or vertical component of receiver n. The spectral density matrix in this case is $\mathbf{S}_{3C} = \langle \mathbf{s}_{3C} \cdot \mathbf{s}_{3C}^{\dagger} \rangle$. The plane wave model of the single-component array can now be extended to include a polarization. For a single receiver in the frequency domain, such a polarization corresponds to three sinusoids on the three components with varying phases and amplitudes. These phases and amplitudes can be described by a complex three-dimensional vector $\mathbf{c} = [c_E, c_N, c_V]^T$ [*Samson*, 1983], where again the subscripts stand for the east, north, and vertical components. For a laterally homogeneous and isotropic medium and a remote source, only certain polarization states can propagate: retrograde/prograde Rayleigh, SH, SV, and *P* wave polarizations. Rayleigh wave states are elliptical within the vertical plane of propagation, with the major axes aligned horizontally or vertically. They are parameterized by their degree of ellipticity which can be described by the ratio of the length of the horizontal major axis to the vertical major axis, sometimes called the H/V ratio. *P* and SV polarizations are parameterized by a dip angle ψ. Since there is only one SH polarization state, no parameterization is necessary there. Table 1 gives the parameter ranges

Table 1. Parameterizations Employed in the Array Processing for the Various Polarization States[a]

Polarization Type	Parameter	Value Range
Rayleigh	H/V ratio	Inf,5,2.5,1.67,1.25,1,0.8,0.6,0.4,0.2,0
	orientation	prograde/retrograde
SH	no parameter	n/a
P	dip angle	0...90° in 2.5° steps
SV	dip angle	0...90° in 2.5° steps

[a]A total of 91 polarization states were used at each wave vector.

of all 91 polarization states used in this study, and Figure 3 illustrates two surface wave polarizations from this set. We describe the parameters of the polarization with ξ, and the resulting three component phase shifts are $c(\xi)$. Since the length of **c** does not affect the described polarization, it can be set to have unit length. The resulting signal model is written as

$$\mathbf{x}(\mathbf{r}, t) = A \cdot \mathbf{c}(\xi) \cdot \exp[2\pi i (\mathbf{k} \cdot \mathbf{r} - ft)], \quad (5)$$

where **x** is now a three-component time series describing particle motion velocity at location **r**. Again, A is a complex scalar describing the amplitude and phase of the plane wave. Note that in equation (5) the polarization ξ is modeled independently from the wave vector **k**. The relative phase variations of a fixed component, say east, among all M sensors therefore only depend on the wave vector and are still captured by the mode vector **a(k)**. On the other hand, the relative phase variations between the three components due to polarization are the same for all receiver locations in this model. The $3 \cdot M$-dimensional, complex mode vector of the array can thus be written as

$$\mathbf{w}(\mathbf{k}, \xi) = \mathbf{c}(\xi) \otimes \mathbf{a}(\mathbf{k}), \quad (6)$$

with $\otimes$ being the Kronecker product. The first M elements of **w** describe the phase responses of all East components in the array, the next M elements those of the north components, and the last M elements those of the vertical components (the receiver order being the same for all components). Note that because both **a** and **c** are normalized, also **w** has unit length. As in the single-component case, the conventional
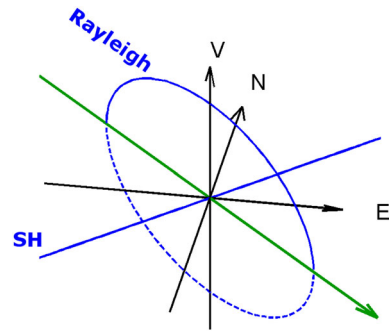

Figure 3. One Rayleigh and one SH polarization states are illustrated for a plane wave propagating from NW to SE. The elliptical Rayleigh states can have prograde (forward movement from top) and retrograde (backward movement from top) motion.

4

beamforming response as a function of wave vector **k** and polarization parameters ξ is

$$R(\mathbf{k}, \xi) = \mathbf{w}(\mathbf{k}, \xi)^\dagger \cdot \mathbf{S}_{3C} \cdot \mathbf{w}(\mathbf{k}, \xi). \qquad (7)$$

[17] Again, the response $R(\mathbf{k}, \xi)$ is maximized when **k** and ξ match with the parameters of an actual plane wave impinging on the array. This also holds when there are several coherent waves because the mathematical representation of the extended model here is formally identical to the single-component case.

[18] Each of the three components of the M receivers is segmented into 40.96 s windows, overlapping by 20.48 sec. We then compute $\mathbf{s}_{3C}$ using the Fast Fourier Transform [*Press*, 2007]. For a given frequency bin, f_0, we estimate $\mathbf{S}_{3C} = \langle \mathbf{s}_{3C} \cdot \mathbf{s}_{3C}^\dagger \rangle$ using block averaging [*Press*, 2007] over 15 consecutive time windows, corresponding to a total window length of ~5 min.

[19] The array coherence $R(\mathbf{k}, \xi)$ equation (7) is computed over a discretized wave vector and polarization space. For the wave vector a polar grid is used with wave numbers ranging from 0.0056 to 0.45 km^{-1} in steps of 0.0056 km^{-1} and with propagation azimuth steps of 5°. We follow the convention of 0° for North and positive angles indicating clockwise rotation.

[20] The parameter space is thus discretized into 5760 wave vectors, with each wave vector connected to the 91 polarization states shown in table 1. The coherence R is now evaluated for each of the $5760 \cdot 91$ joint states. For each wave vector the maximum coherence over all polarizations at that wave vector is stored as well as the polarization that caused it. Figure 4 shows the resulting maximum coherence over the wave vector space for a sample time window at 0.73 Hz. To facilitate interpretation, the wave numbers were scaled to represent slowness as $s = 1/v = k/f$ (v is the phase velocity) and the azimuth angles represent back azimuth (propagation azimuth +180°). The spectrum shown here is different from spectra computed using single-component beamforming because each peak in the slowness spectrum may correspond to another polarization state, depending on what polarization maximized the coherence. In order to capture not just the dominating wave train but also weaker ones, the strongest three peaks in the combined wave vector and polarization space are selected for further analysis. The slowness spectrum shown in Figure 4 is typical for the observations made at the site in that a few clear peaks were visible in most time windows. For the time scale of the analysis window (5 min), it appears that a few distinct sources mostly dominated the wave field. When more than one coherent signal is present, the coherence becomes a biased measure of the seismic power of the signal [*Capon*, 1969]. We follow the procedure described in *Schmidt* [1986] equation (7) to estimate the power for the coherent signals as well as an assumed incoherent noise. This also allows us to assess the signal-to-noise ratio of the detections.

[21] The above process is applied to all Fourier frequencies from 0.1 to 1.1 Hz and then repeated for a window about 2.5 min further ahead in time. The array response shown in Figure 2 contains small side lobes where seismic energy could leak in the analysis with an attenuation of slightly more than 12 dB. Despite that attenuation, these side lobes can lead to strong spectral leakage when the wave
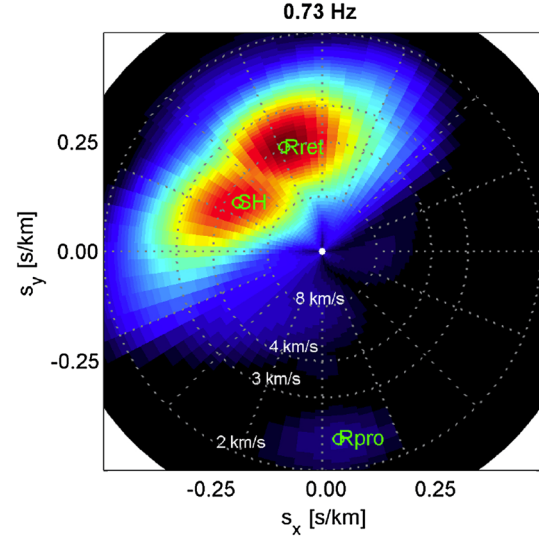

Figure 4. Slowness spectrum at 0.73 Hz for a sample time window centered around 20 April 14:45 h local time. For the three strongest peaks, the polarization that was associated with the response is given (SH: transverse linear, Rret/Rpro: retrograde/prograde Rayleigh).

field is actually dominated by one single-wave train, which was often the case below 0.3 Hz. To reduce such spurious peaks below 0.3 Hz, we discard detections that were more than 50% weaker than the strongest response for frequencies below 0.3 Hz. The resulting database of detections over the 65 h and 55 h recording periods in April and November 2010 will be visualized in the next section.

[22] We also tested the high-resolution beamforming techniques proposed by Capon [*Capon*, 1969] and *Schmidt* [1986] and found very similar results, confirming the statement by [*Koper et al.*, 2010] that for a statistical characterization of wave field properties the choice of the array-processing scheme is not critical.

3.3. Signal Mixtures and Polarization Perturbations

[23] At any given time there might be more than just one dominantly coherent wave train impinging on the array. The processing must be able to properly detect such mixtures with little bias. Also, anisotropy and lateral heterogeneity in the subsurface can cause polarizations to deviate from the isotropic polarization states defined above. One known phenomenon is a deviation of polarization angle and propagation direction [e.g., *Maupin and Park*, 2007]. We assess the performance of the array processor in these two situations using synthetic stochastic signals.

[24] We considered the following scenario. A mixture of three polarized plane waves (without anisotropy effects) impinges on the array: (1) a retrograde Rayleigh wave with H/V amplitude ratio 2.5, traveling at 2.4 km·s^{-1} from direction −15° (~NNW), (2) a prograde Rayleigh wave with H/V ratio 1, traveling at 3.5 km·s^{-1} from back azimuth −70° (~WNW), and (3) a Love wave traveling at 2.8 km·s^{-1} from back azimuth −120° (~WSW). The time signatures of the three plane waves are Gaussian stochastic processes which are independent of each other. Random, spatially white, and unpolarized Gaussian noise was added to the entire setup.
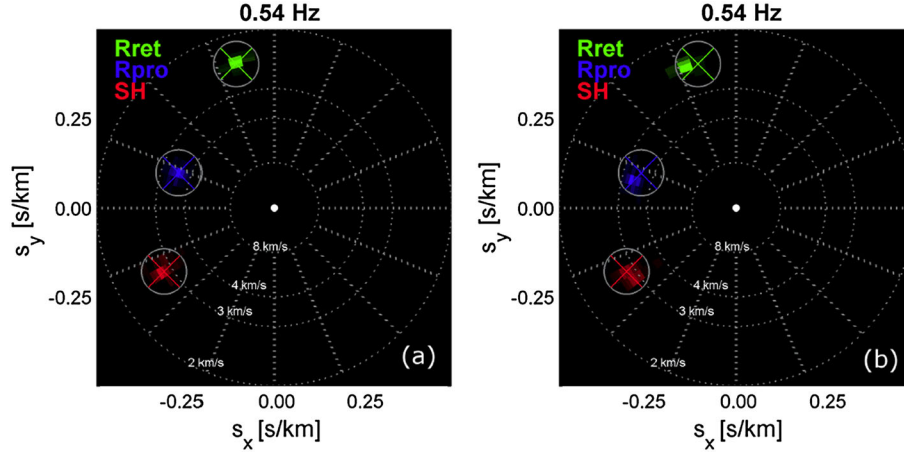
Figure 5. (a) Distribution of detections on 100 realizations of a synthetic mixture of three signals with signal-to-noise ratio 0.25 (see text for details). The crosses indicate the true simulated slowness and back azimuths. The signals are correctly separated. (b) Same as in Figure fig:SynthSpectruma, but the particle motion of the plane waves was rotated along the vertical axis by 20° counterclockwise. Rayleigh and Love polarization thus substantially differs from the isotropic state assumed by the array processor. The effect on estimated slowness is small, but the back azimuths show a bias of 5° counterclockwise.

The simulation was done entirely in the frequency domain for a test frequency of 0.54 Hz. For each time window we simulated the frequency domain amplitudes of the three waves and the added noise by independently and uniformly drawing four amplitudes from a circularly symmetric complex normal distribution (these amplitudes correspond to the term A in equation (4)). The frequency domain amplitudes were scaled such that in the time domain, the expected signal amplitudes were equal and the ratio of the expected signal amplitudes to the expected noise amplitude was 0.25.

[25] We simulated 100 realizations of the above synthetic signal model and processed them with the parameters given in the previous section. The resulting distribution of detections is given in Figure 5a. The processor correctly identified all signals and their wave type. Most of the detections were made within the correct grid point in back azimuth and slowness.

[26] Next, we rotated the particle motion by 20° counterclockwise around the vertical axis to construct out-of-plane polarization. This emulates a situation where lateral heterogeneity and/or anisotropy create polarization states that deviate substantially from the states that can propagate in a simplified model. Again, 100 realizations of spectral density matrices from these distorted signals were simulated and processed with the algorithm. Figure 5b shows the distribution of the resulting detections. The signals are still detected and properly identified, but there is a systematic bias in the back azimuth by about 5°.

[27] The synthetic data used above represent perfect plane wave trains which are stochastically independent in time. In the real data, such signals are unlikely to be encountered in this purity due to scattering, attenuation, multipathing, and other phenomena. A detailed discussion of such effects would go beyond the scope of this test, but we mention them here to be clear about the limitations of the synthetic setup. However, the results qualitatively show that conventional beamforming can be used to characterize signal mixtures and that the isotropic polarization subspace is sufficient to classify Love and Rayleigh waves with moderate polarization perturbations. There is a small but significant estimation bias in back azimuth which should be kept in mind when analyzing surface wave anisotropy (see discussion). When two peaks in the slowness plane are too closely spaced, they can merge into one peak. This limits the angular resolution of the beamformer but could also affect the estimated phase velocity. One controlling factor for angular resolution is the size of the main lobe in the array response shown in Figure 2. For the array geometry available in this study, the angular resolution was about 15°.

4. Overview of Detections

[28] The 65 h and 55 h data sets in April and November 2010 provided 1681 and 1411 time windows, respectively, yielding a total of more than $280 \cdot 10^3$ detections over all 38 frequency bins between 0.2 and 1.1 Hz. Five earthquakes with moment magnitude $M > 5$ occurred during data acquisition. They were teleseismic events and did not dominate the signal. Since we will analyze time distributions of the wave train parameters, their influence would be negligible anyway, because they would affect less than 1% of the time windows. The UGS was operational during the data acquisition phases and can produce large amounts of seismic noise at high frequencies. This noise has been studied (not shown), but no clear signs of infrastructure noise were found below 1.1 Hz. In the following, we give a brief overview of the detections in three different frequency bands for both snapshots. Back azimuths are given with their geographical abbreviation, according to the inlet in Figure 1.

[29] Figure 6a shows a 2-D histogram over the slowness back azimuth polar grid of all detections in April with Rayleigh and SH wave polarizations at 0.22 Hz, corresponding to a frequency almost at the spectral peak of the ocean microseism. The histograms were computed separately for each polarization type, and a composite color spectrum was produced (red for SH/Love, green for retrograde Rayleigh, and blue for prograde Rayleigh). Figure 6b shows the same visualization for the November data. The microseism peak
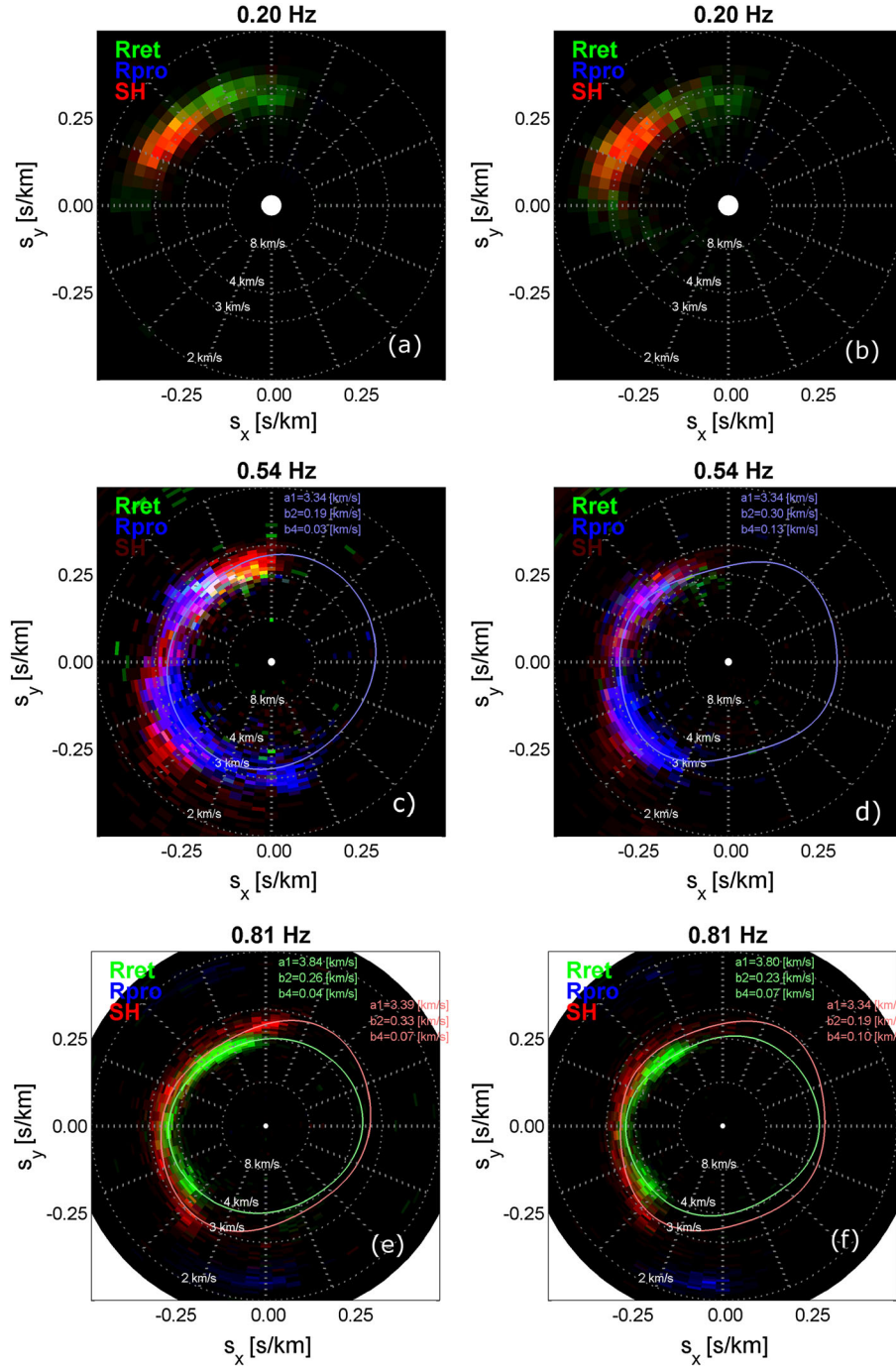
Figure 6. Distribution of detections in the phase slowness plane for various frequencies. (a, c, e) Results for the April snapshot for 0.20 Hz, 0.54 Hz, and 0.81 Hz, respectively. Colors identify the dominant wave type of the detections in each slowness back azimuth bin: green and blue for retrograde/prograde Rayleigh waves and red for SH/Love waves. The lines show the best fit of equation (8) to the data (see section 5). (b, d, f) Results for the November snapshot for 0.20 Hz, 0.54 Hz, and 0.81 Hz, respectively.

consists of both Rayleigh and Love waves, but the mixture is a function of back azimuth. Love waves dominate from WNW, while retrograde Rayleigh waves dominate from NNW directions. Although the slowness resolution is relatively poor at these low frequencies, the Rayleigh waves seem to propagate slightly faster compared to the Love waves. These patterns vary little in the two snapshots. Note that waves in this frequency band are generated by

ocean gravity waves both near coasts and in the deep ocean [*Ardhuin et al.*, 2011; *Hillers et al.*, 2012]. The source area cannot be unambiguously inferred with this analysis.

[30] Figures 6c and 6d show the same visualizations for the frequency bin 0.54 Hz. Prograde Rayleigh waves have a wide range of back azimuths from South to NW (clockwise). In contrast to the April snapshot, the November snapshot shows fewer detections from North and South.

The phase slowness estimations for Love waves are much more scattered than those for the Rayleigh waves which suggest problems with the beamforming algorithm for this frequency and polarization. The brightness of the Love wave histogram has therefore been lowered to emphasize the more stable Rayleigh wave detections. There is evidence for phase velocity anisotropy: energy from the NNW shows lower slowness (i.e., higher velocity) compared to other directions. The solid line is a fit of anisotropy parameters to the slowness detections and is discussed in detail in section 5. Note that the best fit differs visibly between the snapshots.

[31] Figures 6e and 6f show the same visualizations for the frequency bin 0.81 Hz. Phase slowness is much better constrained for both snapshots, and both Love and Rayleigh waves have a wide azimuthal distribution, although their relative proportions still vary by back azimuth. Fewer detections are made from south to SSW (clockwise). The November snapshot has fewer detections from North compared to the April snapshot. Anisotropy in phase velocity is apparent for Rayleigh and Love detections with a fast axis roughly along the NNW-SSE axis. Again, the solid line is a fit of anisotropy parameters to the slowness detections.

[32] Overall, detections above 0.4 Hz show a wider range of back azimuths compared to the microseism peak frequencies. The seasonal snapshots are relatively similar in their main features. No detections were made from the inland directions (NE-SE, clockwise), and only very few detections were made from the North Sea (NNE) and the Mediterranean Sea (SSE). Anisotropy in surface wave phase velocities is consistently observed with different magnitude over all frequency bands and for both seasonal snapshots. This surface wave anisotropy is quantified in the next section.

5. Estimation of Anisotropy Parameters

[33] A visual inspection of Figure 6 shows that the surface wave phase velocities vary with back azimuth over a wide range of frequencies. One likely explanation for such a phenomenon is anisotropy in the seismic parameters of the subsurface. *Smith and Dahlen* [1973] showed that for a stratified half space, such anisotropy would at first order cause a variation of surface wave phase velocities as follows:

$$v(\theta) = a_0 + a_1 \cos(2\theta) + a_2 \sin(2\theta) + a_3 \cos(4\theta) + a_4 \sin(4\theta), \quad (8)$$

where v is the surface wave phase velocity (km·s^{-1}), θ is the direction of propagation measured clockwise from north, and a_i are parameters that depend on the subsurface. In this formulation, the magnitude of the 2θ and 4θ terms are

$$b_{2\theta} = \sqrt{a_1^2 + a_2^2},$$
$$b_{4\theta} = \sqrt{a_3^2 + a_4^2}. \quad (9)$$

[34] Figures 7a–7c show the observed distribution of phase velocity as a function of back azimuth over the population of all April detections of Rayleigh waves at 0.54 Hz and Rayleigh and Love waves at 0.81 Hz, respectively. A clear azimuthal pattern in the detections can be made out in these plots. The histogram bins stretch along the velocity axis with higher velocities which is due to the fact that the array processor response was computed on an even grid in slowness rather than phase velocity. To quantify the velocity
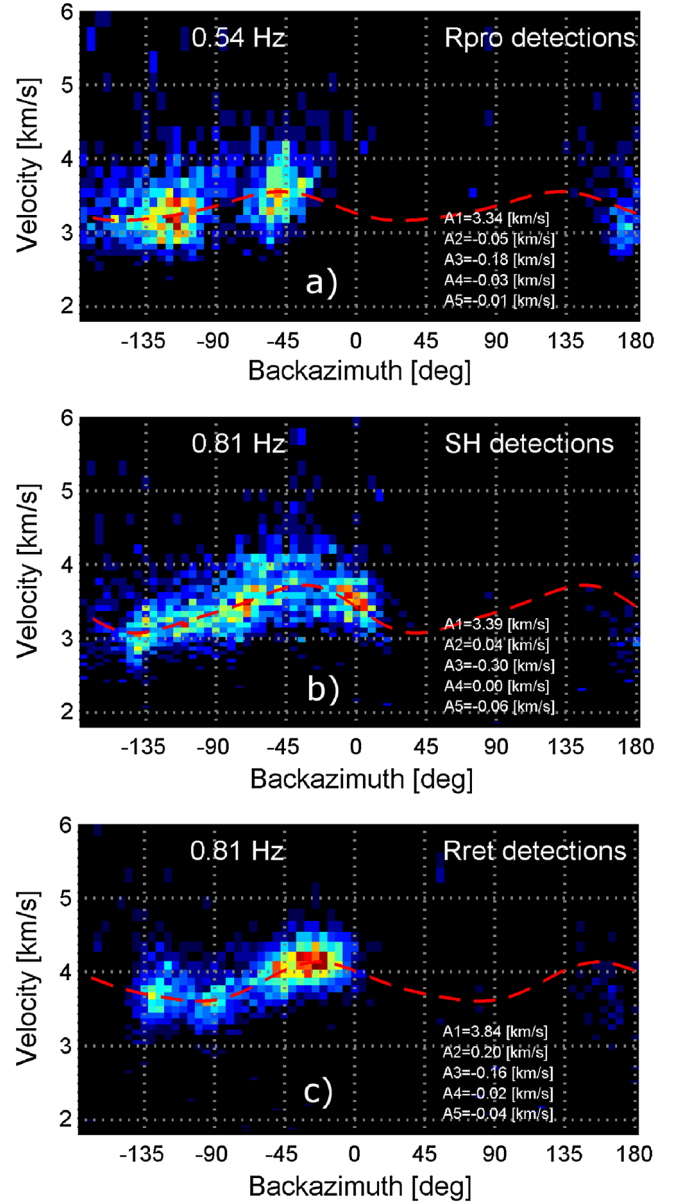

Figure 7. Two-dimensional histograms over the slowness back azimuth space are computed for (a) 0.54 Hz and Rayleigh polarization, (b) 0.81 Hz and SH polarization, and (c) 0.81 Hz and Rayleigh polarization. The dashed red lines indicate the best fit of equation (8), with the coefficients shown on the bottom right.

anisotropy for a given frequency and polarization type, we fit the *Smith and Dahlen* [1973] model on this data. Figure 7a at 0.54 Hz shows an example of suboptimal azimuthal illumination, while the other examples are better in this respect. Note that the distribution of velocities is nonsymmetric with a heavy tail toward high velocities, in particular in Figures 7a and 7b. Such non-Gaussian distributions can lead to substantial bias in a conventional least squares fitting procedure. We therefore use the more robust least absolute deviations approach which minimizes the sum of absolute deviations rather than their squares [*Bloomfield and Steiger*, 1983]. The resulting best fits are shown in Figure 7 as dashed red lines with the best fit parameters given at the bottom right.
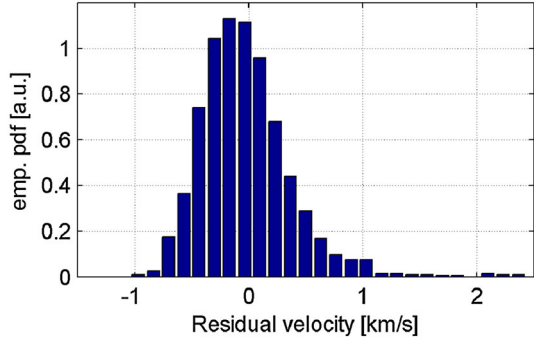
Figure 8. Empirical probability distribution of the residuals from the fit to the 0.54 Hz Rayleigh wave data. The distribution is asymmetric and has a heavy upward tail.

Visual inspection confirms that the fitting routine behaves as expected. Figure 8 shows the residuals from the fit and confirms both the asymmetric character and heavy upward tail of the distribution underlying the velocity estimates.

[35] The 4θ parameters (a_3, a_4) are relatively small, and the question arises as to their significance. We assess the uncertainty in the fit parameters as well as their statistical significance by recomputing the fitting process on bootstrap resamples of the data [*Efron and Tibshirani*, 1993]. This process in effect attempts to estimate the sampling distribution of the actual anisotropy parameters given the observed variability in the velocity estimates. Starting out from N azimuth and phase velocity pairs at a given frequency bin and polarization, we randomly sample (with replacement) an equally large set of N data points. The *Smith and Dahlen* [1973] model parameters are estimated using the above-fitting routine, and the entire process is repeated B times. This random resampling mimics the variability in the data and allows one to see how this variability is inherited by the anisotropy parameter estimates. The optimal number B of resamples is a function of the true variability in the data and the structure of the hypothesis test. We defined it heuristically by using different numbers from $B = 10$ to 1000 and taking the value above which the main features of the bootstrap distribution seize to change substantially. This criterion was attained at $B = 100$. Figure 9a shows $B = 100$ bootstrap estimates of the four anisotropy parameters (a_1, a_2) (2θ terms) and (a_3, a_4) (4θ terms) for 0.81 Hz and retrograde Rayleigh polarization, all given as a percentage relative to the isotropic phase velocity a_0. The elongated, diagonal shape of the distribution of the 2θ parameters is evidence that the parameter estimations can be correlated. If the true 4θ terms were zero, the (a_3, a_4) parameters would be distributed around the origin. Note that the distribution of the magnitude $b_{4\theta}$ is always positive, also in the case of $(a_3 = a_4 = 0)$, and no symmetric significance test can be used on it. To account for the latter two facts, we test statistical significance in the two-dimensional (a_1, a_2) or (a_3, a_4) space, following a procedure described in *Liu et al.* [1999]: a convex hull is computed around the 90% of estimations that lie within the center of the (a_1, a_2) and (a_3, a_4) data clouds as defined by the Mahalanobis depth [*Liu et al.*, 1999]. The Mahalanobis depth in this case accounts for the asymmetry in the parameter distributions that was observed in many cases. The convex hulls are shown for the 2θ and 4θ parameters in Figure 9a. If the

origin (0,0) lies within the convex hull, the parameters are considered statistically insignificant at 90% level. Both the 2θ and 4θ terms are therefore statistically significant at the 90% level. Figure 9b shows the same graph for the 0.54 Hz bin and prograde Rayleigh polarization, hence the less well constrained example shown in Figure 7a. Here the 2θ term is still statistically significant at 90% confidence, but this is no longer true for the 4θ term.

[36] We repeat the above process for every Fourier bin in the analyzed frequency range and for all polarization types. The analysis was restricted to subsets that exhibit a
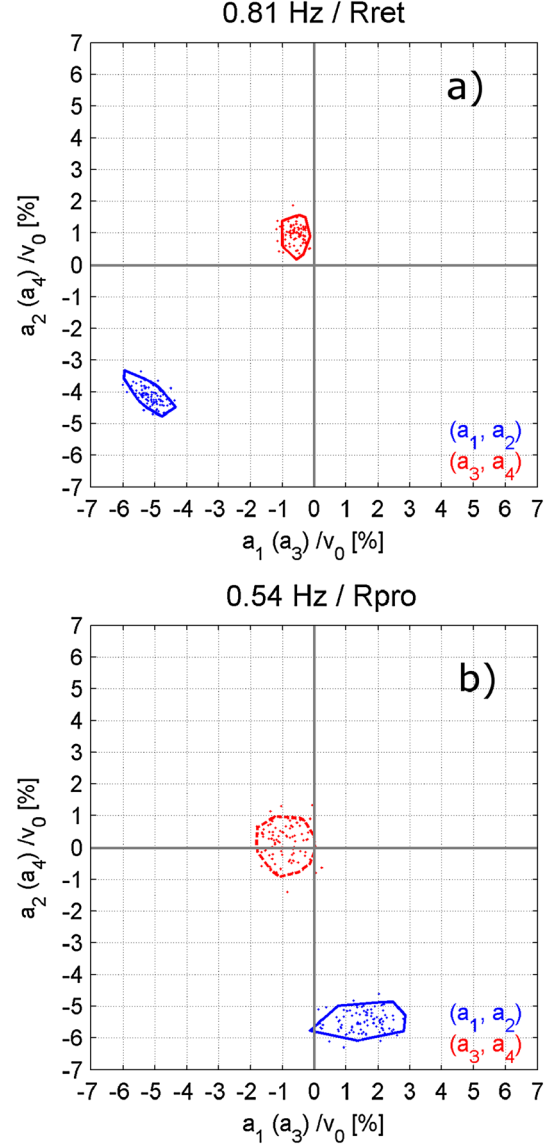

Figure 9. (a) Using bootstrap resamples, 100 estimations of (a_1, a_2) and (a_3, a_4) were made at 0.81 Hz and SH polarization. The point clouds visualize the estimations and show that the 2θ (blue) and 4θ (red) terms are significant at 90% confidence, with the latter being much smaller. The polygons delineate the convex hull containing the inner 90% of data points. (b) The same visualization as in Figure 9a for 0.54 Hz and prograde Rayleigh motion. The convex hull of the 4θ point cloud contains $(a_3, a_4) = (0, 0)$ and thus is not significant at the 90% level.
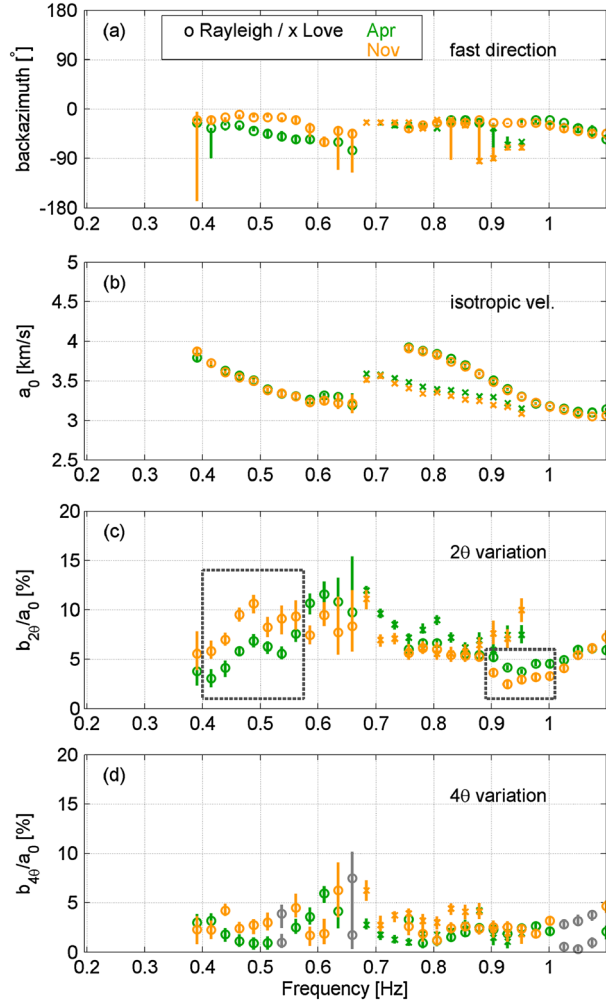
Figure 10. Spectra of the parameters from the fitting procedure for the April data (green) and November data (orange). The vertical bars indicate the range within which 90% of the bootstrap estimates lie. Estimates for Rayleigh waves are marked by crosses, those for Love waves by circles. (a) Spectrum of the direction of fastest phase velocity. (b) Spectrum of the isotropic term a_0 from equation (8). (c) Spectrum of $b_{2\theta}$ term. (d) Spectrum of $b_{4\theta}$ term. Gray color indicates estimations that are not statistically significant at the 90% level. Note how in those cases the vertical bars cannot necessarily be used for significance testing. The dashed boxes in Figure 10b are discussed in the text.

back azimuth range wider than $100°$ and where there was no evidence of different surface wave modes of the same polarization being present. The latter is done by avoiding frequency bins and polarizations where we observe two different phase slownesses from the same back azimuth or sudden changes in phase slowness as a function of back azimuth. The best fitting models are superimposed as solid lines on the slowness spectra in Figure 6.

[37] The above procedure produces spectra for (1) the direction of fastest phase velocity, (2) the isotropic phase velocity a_0, (3) the anisotropy term $b_{2\theta}$, and (4) the anisotropy term $b_{4\theta}$ as defined in equation (9). Figures 10a–10d show these four spectra for the April and November data, with different colors used to identify the two snapshots.

Estimations that did not provide visually acceptable fits were not included in the figure.

[38] A striking feature in Figure 10a is the fact that above 0.7 Hz, both Love and Rayleigh waves have a relatively constant fast direction up to more than 1 Hz, a feature that is visible in both snapshots. In this frequency band the fast direction lies within a back azimuth range of $–35°$ to $–20°$ for both the Rayleigh and Love mode. For the prograde Rayleigh mode below 0.7 Hz, this fast direction is less constant over frequency and varies between $–60°$ and $–10°$. These fast directions (NNW-SSE) are roughly aligned with the preferred fault orientation of shallow (<300 m) and deeper (~ 1 km) fault systems described by *Sala et al.* [2013] and shown in Figure 1. Below 0.6 Hz the fast direction of the November data has a more northward trend compared to the April data.

[39] Figure 10b shows the best fitting isotropic dispersion curves for the observed surface waves. Three distinct branches are visible, clearly separated by polarization and phase velocity. These branches probably correspond to three surface wave modes. While the Rayleigh wave velocities match between the snapshots, the Love wave velocities are consistently slower in November by between 10 and 100 m/s.

[40] Figures 10c and 10d are a quantitative estimates of the 2θ and 4θ terms, respectively. Markers in gray indicate estimates that were not statistically significant at the 90% level. It is clear that the 2θ term is stronger over most of the frequency band. But the 4θ estimations in most frequency bins are still statistically significant at 90% confidence. Both terms seem to depend primarily on frequency and less so on the polarization of the surface waves. The inappropriateness of using the variability of anisotropy magnitudes for significance testing is made obvious here: the 90% variation range (vertical bars) do not contain zero even where there is no statistical significance.
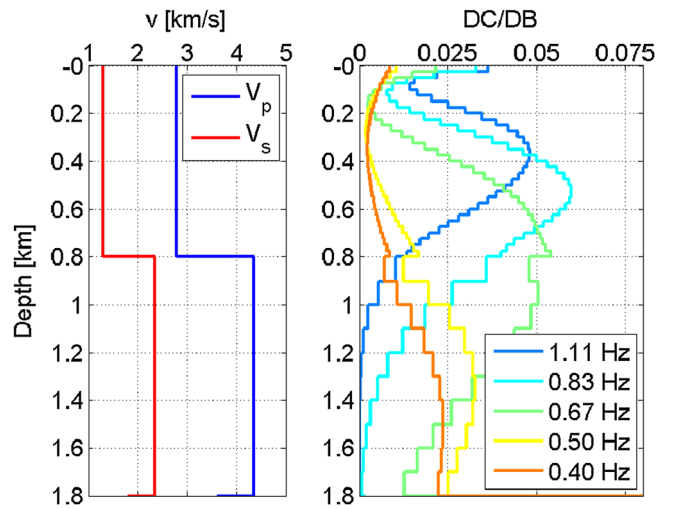

Figure 11. (a) Simplified velocity profile for the Paris Basin based on well data from *Bush and Crampin* [1991]. (b) Depth sensitivity kernels for phase velocity of Rayleigh wave fundamental modes at five different frequencies within the analyzed band.

[41] Comparing the 2θ anisotropy in Figure 10c for the two snapshots, we note certain features: between 0.6 and 0.85 Hz, the Rayleigh wave anisotropy roughly matches within the 90% variability ranges. Above 0.9 Hz there is a small decrease of 1–2% for November (dashed box to the right). On the other hand, below 0.6 Hz we observe an increase of anisotropy by 3–5% (dashed box to the left). This coincides with the mismatch observed for the fast direction in Figure 10a. Love wave anisotropy does not change between 0.85 and 0.95 Hz but is lower in November by about 1–3% between 0.7 and 0.85 Hz. The 4θ terms are stronger in November for almost all frequency bins. The observed patterns are discussed in the following section.

6. Discussion

[42] We have presented a three-component seismic array-processing scheme with which phase velocity and back azimuth of ambient Rayleigh and Love waves can be captured. Ambient surface waves in the frequency range between the secondary ocean microseism peak at 0.2 Hz up to 1.1 Hz were characterized for two snapshots in April and November 2010. The microseism peak energy at 0.2 Hz consists of similar proportions of Love and Rayleigh wave detections coming from a narrow range of back azimuths. However, around 0.4 Hz we observe that higher-surface wave modes start to dominate the wave field (Figure 10b) with a concurrent widening of the range of back azimuths (Figures 6c–6f). The increased back azimuth range might be due to higher-frequency surface wave scattering on heterogeneities. On the other hand, it is also conceivable that the particular conditions under which ocean gravity waves and the solid earth interact to produce surface waves are satisfied on more locations at higher frequencies.

[43] The array processor assumes isotropic polarization states, while the observations show obvious anisotropy in the wave field. However, as tested in section 3.3, the sensitivity of the estimator to polarization perturbations seems rather limited and the bias in back azimuth should be small enough to not affect the anisotropy results shown in this study. The clear identification of three surface wave branches in the dispersion curves of Figure 10b are further evidence that perturbations in Rayleigh and Love wave polarization are probably not too strong. But such perturbations can still be included in the array processor and might provide additional constraints on the anisotropy in the subsurface [*Tanimoto*, 2004] although this must be done with caution [*Maupin*, 2004].

[44] Anisotropy was quantified by fitting the *Smith and Dahlen* [1973] model to the data at every frequency bin and for Love and Rayleigh waves separately. Using least absolute deviations rather than least squares accounts for the non-Gaussian, heavy-tailed distribution of the phase slowness estimations from the array processing. We approximated the distribution of the anisotropy parameter estimations by a bootstrap distribution and also showed evidence of correlation among the (a_1, a_2) (2θ terms) and (a_3, a_4) (4θ terms) parameter estimates. The resulting uncertainties and significance tests on the anisotropy parameters capture uncertainties due to the velocity estimation variability, though they do not account for systematic bias in the beamformer detections.

[45] From Figures 10a and 10b we see that the fast direction and the isotropic part of the phase velocities are relatively stable between the two snapshots with two exceptions: the fast direction has northward trends in November between 0.45 and 0.6 Hz, and Love wave phase velocities were found to be consistently lower in November compared to April. For an area in Japan, *Nakata and Snieder* [2012] observed that shear wave velocity within less than 500 m depth could be lowered by an increase in precipitation. Although they studied higher frequencies (1–13 Hz) than in this analysis, precipitation may still be a plausible cause of the lower Love wave velocities.

[46] The 2θ variation (Figure 10c) between 0.4 and 0.6 Hz are higher in November compared to April by about 3–5%, while at 0.9–1.0 Hz they are lower by about 1–2%. The weaker 4θ terms (Figure 10d) were mostly estimated at higher levels in November.

[47] There are several potential explanations for the differences between the snapshots. Diffraction and mode interference will in all likelihood introduce unknown estimation bias within and between the snapshots, and the bootstrap uncertainties and significance tests do not address this bias. The orientation of the sensors was done manually using hand compasses which is another potential source of bias. The latter error source would presumably have a random character, and it is therefore unlikely that the observed difference between spring and autumn would be produced by it.

[48] Perhaps the most interesting difference, however, is that of the subsurface itself. As mentioned above, differences in precipitation between the seasons might affect the shallow subsurface which could explain the 2θ variations at higher frequencies (right box in Figure 10c). Also, the state of the UGS, above which the measurements took place, was distinctly different between the snapshots. In April it was mostly depleted due to Winter demand with minimum pore pressure. In November, on the other hand, it was close to its maximum fill with accordingly high pore pressure. The increased pore pressure might lead to an extension of fractures and/or cracks in the reservoir interval, thereby pronouncing the existing effect of the fault system on surface wave anisotropy. For instance, *Tonegawa et al.* [2013] used an oblate spheroidal crack model where changes in the crack aspect ratios explained variations in *S* wave anisotropy in shallow marine sediments. Considering the depth of the reservoir, this explanation might be more pertinent to the Rayleigh wave anisotropy variations below 0.6 Hz (left box in Figure 10c). Another potential source of variation is the overburden. *Teatini et al.* [2011] described cyclic subsidence and uplift on the vertical and horizontal component above a gas storage facility in the Po plain in Italy. Geomechanical effects on such a large scale might change effective anisotropy measurably. Both explanations are, in general, consistent with the near-constant fast direction between 0.4 and 1.1 Hz which matches the preferred direction of both shallow (<300 m) and deeper (1 km) fault systems as shown in Figure 1. That orientation also corresponds to the orientation of maximum compressive horizontal stress (e.g., World Stress Map, www.world-stress-map.org).

[49] We want to qualitatively assess the plausibility whether pore pressure changes in the reservoir could be responsible for the observed anisotropy change at 0.4–0.6 Hz. To this end, we compute depth sensitivity kernels

[*Herrmann*, 1996] for surface waves at various frequencies of our observed anisotropy range. *Bush and Crampin* [1991] published a profile of seismic velocity and density from a well in the Paris Basin that reached down to 2.8 km. We use a simplified version of that profile in Figure 11a which gives the V_p and V_s depth profile for the top 1.8 km, to calculate partial derivatives of phase velocity with respect to changes of in situ shear wave velocity. We do not consider the dependence on compressional velocity or density, since they are much weaker. The resulting depth sensitivity kernels for Rayleigh waves are shown in Figure 11b. The depth range to which phase velocities are sensitive generally become shallower with increasing frequency. The higher frequencies in this study for which we do not detect any differences are sensitive to the topmost kilometer. The frequencies 0.67 Hz, 0.50 Hz, and 0.4 Hz, where we notice different anisotropic parameters between spring and autumn, have considerable sensitivity to the depth range 1000–1200 m where the reservoir is located. This suggests that the temporal variation of seismic anisotropy might be caused by the different pore pressures in the reservoir between spring and autumn. However, our test only computes sensitivity to shear wave velocity and not to azimuthal anisotropy directly. That the reservoir interval is responsible for the observed changes therefore remains speculative. Future research could attempt to invert the spectra of anisotropy parameters underlying Figure 10 for anisotropy in the subsurface [*Montagner and Nataf*, 1986]. Since both Love and Rayleigh waves are detected, such a scheme could also take advantage of Love-Rayleigh wave discrepancies to address vertical transverse isotropy. Although the beamformer in this study was not optimized for it, the H/V ratio could be used as another wave field parameter to interpret for the cause of the variation.

[50] Finally, the type of seismic anisotropy that we observe here is generally consistent with the orientation of fractures in the area, which also corresponds to the orientation of the maximum horizontal stress in the area. Opening of fractures and cracks can have a significant effect on seismic anisotropy, but the precise mechanism is beyond the scope of this paper.

7. Conclusions

[51] We used data from a temporary three-component seismic array in the Paris Basin to characterize ambient Love and Rayleigh waves in terms of their phase velocity distribution as a function of back azimuth. The data was acquired above an underground gas storage during a few days in April and November 2010. The analyzed frequency range of 0.2–1.1 Hz covered the secondary microseism peak and its higher-frequency flank.

[52] For both snapshots the microseism peak was around 0.2 Hz and consisted of both retrograde Rayleigh and Love wave modes with back azimuths distributed between North and West. Above 0.4 Hz, however, higher-surface wave modes started to dominate with a much wider range of back azimuths (∼160°). The *Smith and Dahlen* [1973] equation for surface wave anisotropy fits well to most of the data, and we estimate spectra of its isotropic and anisotropic parameters.

[53] According to a bootstrap test, the Rayleigh waves exhibit substantially higher 2θ anisotropy in November

below 0.6 Hz, increasing from 3–7% to 6–11%. The isotropic part of the phase velocity dispersion for Love and Rayleigh waves, meanwhile, match for both snapshots. We also observe a stable fast direction of NNW-SSE for Love and Rayleigh waves which is aligned with the preferred orientation of shallow (<300 m) and deeper (1000 m) fault systems in the area. We speculate that these observations might be due to geomechanical effects in the reservoir interval caused by increased pore pressure.

References

Adam, J. M. C., and S. Lebedev (2012), Azimuthal anisotropy beneath southern Africa from very broadband surface-wave dispersion measurements, *Geophys. J. Int.*, *191*(1), 155–174.

Alvizuri, C., and T. Tanimoto (2011), Azimuthal anisotropy from array analysis of Rayleigh waves in Southern California, *Geophys. J. Int.*, *186*(3), 1135–1151.

Ardhuin, F., E. Stutzmann, M. Schimmel, and A. Mangeney (2011), Ocean wave sources of seismic noise, *J. Geophys. Res.*, *116*, C09004, doi:10.1029/2011JC006952.

Bear, L. K., G. L. Pavlis, and G. H. R. Bokelmann (1999), Multi-wavelet analysis of three-component seismic arrays: Application to measure effective anisotropy at Pinon Flats, California, *Bull. Seismol. Soc. Am.*, *89*(3), 693–705.

Beccaletto, L., F. Hanot, O. Serrano, and S. Marc (2011), Overview of the subsurface structural pattern of the Paris Basin (France): Insights from the reprocessing and interpretation of regional seismic lines, *Mar. Pet. Geol.*, *28*(4), 861–879.

Bloomfield, P., and W. L. Steiger (1983), *Least Absolute Deviations: Theory, Applications, and Algorithms*, Progress in Probability and Statistics, xiv, 349 pp., Birkhauser, Boston, Mass.

Bokelmann, G. H. R. (1995), P-wave array polarization analysis and effective anisotropy of the brittle crust, *Geophys. J. Int.*, *120*(1), 145–162.

Bromirski, P. D., and F. K. Duennebier (2002), The near-coastal microseism spectrum: Spatial and temporal wave climate relationships, *J. Geophys. Res.*, *107*(B8), ESE 5-1–ESE 5-20, doi:10.1029/2001JB000265.

Bush, I., and S. Crampin (1991), Paris Basin VSPs - case-history establishing combinations of fine-layer (or lithologic) anisotropy and crack anisotropy from modeling shear wavefields near point singularities, *Geophys. J. Int.*, *107*(3), 433–447.

Capon, J. (1969), High-resolution frequency-wavenumber spectrum analysis, *Proc. IEEE*, *57*(8), 1408–1418.

Debeglia, N., and S. Debrand Passard (1980), Principaux accidents tectoniques issus des correlations entre les donnes geophysiques et les donnes de terrain dans le Sud-Ouest du Bassin de Paris, *Bull. Soc. Geol. Fr.*, *22*, 639–664.

Durand, S., J. P. Montagner, P. Roux, F. Brenguier, R. M. Nadeau, and Y. Ricard (2011), Passive monitoring of anisotropy change associated with the Parkfield 2004 earthquake, *Geophys. Res. Lett.*, *38*, L13303, doi:10.1029/2011GL047875.

Efron, B., and R. Tibshirani (1993), *An Introduction to the Bootstrap*, Monographs on Statistics and Applied Probability, Chapman and Hall, New York.

Esmersoy, C., V. F. Cormier, and M. N. Toksoz (1985), Three-component array processing, in *The VELA Program : A Twenty-Five Year Review of Basic Research*, edited by A. U. Kerr, xviii, 964 p., Executive Graphic Services, United States.

Fleury, R., F. Charnet, J. Corpel, S. Debrandpassard, Y. Gros, and P. Maget (1997), *Carte gol. France (1/50 000), feuille Romorantin (460)*.

Fry, B., F. Deschamps, E. Kissling, L. Stehly, and D. Giardini (2010), Layered azimuthal anisotropy of Rayleigh wave phase velocities in the European Alpine lithosphere inferred from ambient noise, *Earth Planet. Sci. Lett.*, *297*(1-2), 95–102.

Gallego, A., M. P. Panning, R. M. Russo, D. Comte, V. I. Mocanu, R. E. Murdie, and J. C. Vandecar (2011), Azimuthal anisotropy in the Chile Ridge subduction region retrieved from ambient noise, *Lithosphere*, *3*(6), 393–400.

Gerstoft, P., M. C. Fehler, and K. G. Sabra (2006), When Katrina hit California, *Geophys. Res. Lett.*, *33*, L17308, doi:10.1029/2006GL027270.

Gerstoft, P., P. M. Shearer, N. Harmon, and J. Zhang (2008), Global P, PP, and PKP wave microseisms observed from distant storms, *Geophys. Res. Lett.*, *35*, L23306, doi:10.1029/2008GL036111.

Hamon, Y., and G. Merzeraud (2005), *Nouvelles donnes sur le Trias de Sologne (Chemery, Sud-Ouest du Bassin de Paris): Stratigraphie et environnements de depots,* pp. 3–22.

Herrmann, R. (1996), *Computer Programs in Seismology: 3.0*, Saint Louis University, Saint Louis, Mo.

Hillers, G., N. Graham, M. Campillo, S. Kedar, M. Landes, and N. Shapiro (2012), Global oceanic microseism sources as seen by seismic arrays and predicted by wave action models, *Geochem. Geophys. Geosyst.*, *13*, Q01021, doi:10.1029/2011GC003875.

Kind, F., D. Fah, and D. Giardini (2005), Array measurements of S-wave velocities from ambient vibrations, *Geophys. J. Int.*, *160*(1), 114–126.

Koper, K. D., and B. de Foy (2008), Seasonal anisotropy in short-period seismic noise recorded in South Asia, *Bull. Seismol. Soc. Am.*, *98*(6), 3033–3045.

Koper, K. D., B. de Foy, and H. Benz (2009), Composition and variation of noise recorded at the Yellowknife Seismic Array, 1991–2007, *J. Geophys. Res.*, *114*, B10310, doi:10.1029/2009JB006307.

Koper, K. D., K. Seats, and H. Benz (2010), On the composition of Earth's short-period seismic noise field, *Bull. Seismol. Soc. Am.*, *100*(2), 606–617.

Lacoss, R. T., E. J. Kelly, and M. N. Toksoz (1969), Estimation of seismic noise structure using arrays, *Geophysics*, *34*(1), 21–38.

Landes, M., F. Hubans, N. M. Shapiro, A. Paul, and M. Campillo (2010), Origin of deep ocean microseisms by using teleseismic body waves, *J. Geophys. Res.*, *115*, B05302, doi:10.1029/2009JB006918.

Liu, R. Y., J. M. Parelius, and K. Singh (1999), Multivariate analysis by data depth: Descriptive statistics, graphics and inference, *Annals of Statistics*, *27*(3), 783–840.

Maupin, V. (2004), Comment on 'The azimuthal dependence of surface wave polarization in a slightly anisotropic medium' by T. Tanimoto, *Geophys. J. Int.*, *159*(1), 365–368.

Maupin, V., and J. Park (2007), Theory and observations wave propagation in anisotropic media, in *Treatise on Geophysics*, vol. 1, edited by G. Schubert, pp. 296–300, Elsevier, Amsterdam, Boston.

Montagner, J. P., and H. C. Nataf (1986), A simple method for inverting the azimuthal anisotropy of surface waves, *J. Geophys. Res.*, *91*(B1), 511–520.

Moschetti, M. P., M. H. Ritzwoller, F. Lin, and Y. Yang (2010), Seismic evidence for widespread western US deep-crustal deformation caused by extension, *Nature*, *464*(7290), 885–U94.

Nakata, N., and R. Snieder (2012), Time-lapse change in anisotropy in Japan's near surface after the 2011 Tohoku-Oki earthquake, *Geophys. Res. Lett.*, *39*, L11313, doi:10.1029/2012GL051979.

Parolai, S., M. Picozzi, S. M. Richwalski, and C. Milkereit (2005), Joint inversion of phase velocity dispersion and H/V ratio curves from seismic noise recordings using a genetic algorithm, considering higher modes, *Geophys. Res. Lett.*, *32*, L01303, doi:10.1029/2004GL021115.

Pawlak, A., D. W. Eaton, F. Darbyshire, S. Lebedev, and I. D. Bastow (2012), Crustal anisotropy beneath Hudson Bay from ambient noise tomography: Evidence for post-orogenic lower-crustal flow? *J. Geophys. Res.*, *117*, B08301, doi:10.1029/2011JB009066.

Perrodon, A., and J. Zabek (1990), Paris Basin, in Interior Cratonic Basins, *Am. Assoc. Pet. Geol. Mem.*, *51*, 653–679.

Press, W. H. (2007), *Numerical Recipes: The Art of Scientific Computing* 3rd ed., Cambridge Univ. Press, Cambridge, UK, New York.

Sala, P., M. Frehner, N. Tisato, and O. A. Pfiffner (2013), Building a three-dimensional near-surface geologic and petrophysical model based on borehole data: A case study from Chémery, Paris Basin, France, *AAPG Bull.*, *97*, 1303–1324, doi:10.1306/02261312120.

Samson, J. C. (1983), Pure states, polarized waves, and principal components in the spectra of multiple, geophysical time-series, *Geophys. J. R. Astron. Soc.*, *72*(3), 647–664.

Schaefer, J. F., L. Boschi, T. W. Becker, and E. Kissling (2011), Radial anisotropy in the European mantle: Tomographic studies explored in terms of mantle flow, *Geophys. Res. Lett.*, *38*, L23304, doi:10.1029/2011GL049687.

Scherbaum, F., K. G. Hinzen, M. Ohrnberger, and R. B. Herrmann (2003), Determination of shallow shear wave velocity profiles in the Cologne, Germany area using ambient vibrations, *Geophys. J. Int.*, *152*(3), 597–612.

Schmidt, R. O. (1986), Multiple emitter location and signal parameter estimation, *IEEE Trans. Antennas Propag.*, *34*(3), 276–280.

Shapiro, N. M., M. H. Ritzwoller, P. Molnar, and V. Levin (2004), Thinning and flow of Tibetan crust constrained by seismic anisotropy, *Science*, *305*(5681), 233–236.

Smith, M. L., and F. A. Dahlen (1973), The azimuthal dependence of Love and Rayleigh wave propagation in a slightly anisotropic medium, *J. Geophys. Res.*, *78*(17), 3321–3333.

Takagi, R., and T. Okada (2012), Temporal change in shear velocity and polarization anisotropy related to the 2011 M9.0 Tohoku-Oki earthquake examined using KiK-net vertical array data, *Geophys. Res. Lett.*, *39*, L09310, doi:10.1029/2012GL051342.

Tanimoto, T. (2004), The azimuthal dependence of surface wave polarization in a slightly anisotropic medium, *Geophys. J. Int.*, *156*(1), 73–78.

Teatini, P., et al. (2011), Geomechanical response to seasonal gas storage in depleted reservoirs: A case study in the Po River basin, Italy, *J. Geophys. Res.*, *116*, F02002, doi:10.1029/2010JF001793.

Toksoz, M. N., and R. T. Lacoss (1968), Microseisms: Mode structure and sources, *Science*, *159*(3817), 872–873.

Tonegawa, T., Y. Fukao, K. Nishida, H. Sugioka, and A. Ito (2013), A temporal change of shear wave anisotropy within the marine sedimentary layer associated with the 2011 Tohoku-Oki earthquake, *J. Geophys. Res. Solid Earth*, *118*(2), 607–615, doi:10.1002/jgrb.50074.

Wathelet, M., D. Jongmans, and M. Ohrnberger (2005), Direct inversion of spatial autocorrelation curves with the neighborhood algorithm, *Bull. Seismol. Soc. Am.*, *95*(5), 1787–1800.

Wüstefeld, A., G. Bokelmann, G. Barruol, and J. P. Montagner (2009), Identifying global seismic anisotropy patterns by correlating shear-wave splitting and surface-wave data, *Phys. Earth Planet. Inter.*, *176*(3-4), 198–212.

Zhang, J., P. Gerstoft, and P. M. Shearer (2009), High-frequency P-wave seismic noise driven by ocean winds, *Geophys. Res. Lett.*, *36*, L09302, doi:10.1029/2009GL037761.

Zhang, J. A., P. Gerstoft, and P. D. Bromirski (2010), Pelagic and coastal sources of P-wave microseisms: Generation under tropical cyclones, *Geophys. Res. Lett.*, *37*, L15301, doi:10.1029/2010GL044288.